WELDING RESEARCH

SUPPLEMENT TO THE WELDING JOURNAL, JANUARY, 1982
Sponsored by the American Welding Society and the Welding Research Council

Solidification Cracking and Analytical Electron Microscopy of Austenitic Stainless Steel Weld Metals

Four modes of solidification are possible, and a change in solidification mode from primary delta-ferrite to primary austenite results in an increase in hot-cracking susceptibility

BY M. J. CIESLAK, A. M. RITTER AND W. F. SAVAGE

Introduction

The mechanism of solidification of austenitic stainless steel weld metals and castings is an area of continuing research interest. Hot-cracking has been reported (Ref. 1-5) in several commercial grades when the percentage of ferrite in the microstructure falls below approximately 4%. However, hot-cracking has also been shown (Ref. 3) to be intimately related to the location of ferrite in the microstructure. Room temperature ferrite is found at the cores of the original dendrites in alloys which solidify as primary delta-ferrite, while ferrite is often observed in the interdendritic volumes of alloys which solidify as primary austenite.

Since elements such as sulfur and phosphorus have a higher solubility in delta ferrite than in austenite, a greater proportion of these potentially harmful elements is accommodated in solid solution when ferrite is the primary phase than when austenite is the primary phase. In the latter case, the solubility of these elements in austenite is so low that most of the sulfur and phosphorus is rejected to the last remaining liquid, and thus is concentrated at the dendrite interstices. This segregation of impurities that lower the effective solidus temperature of the last material to solidify promotes hot cracking.

The effect of nitrogen on the ferrite content of austenitic stainless steels has been well documented (Ref. 6-10). Delong, *et al.* have assigned a nickel equivalent of 30 for nitrogen. Kotecki reported (Ref. 8) a decrease in the ferrite content of weldments produced using Type 308, 308L, 309 and 309L flux cored stainless steel welding wire, i.e., electrodes, in the presence of nitrogen.

Arata, *et al.* (Ref. 10) have reported that nitrogen additions to Types 304, 316, and 321 stainless steel weld metal reduced the ferrite number and increased hot-cracking of these alloys. On the other hand, Lundin, *et al.* (Ref. 11) recently reported that nitrogen additions to austenitic stainless steel weld metals had relatively little effect on hot-cracking susceptibility as measured by the fissure bend test. However, this conclusion appears to be based upon autogenous welds in a Type 304L base metal with only 0.004% sulfur, and if so, the low impurity content could account for their results.

Recent work at RPI (Ref. 3) on a series of CF-8M alloys indicated that the hot-cracking susceptibility of this grade increases drastically as the solidification mode changes from one of primary delta ferrite to one of primary austenite. The implication is that any change in the ratio of nickel equivalent to chromium equivalent which causes a shift to primary austenite solidification will increase the susceptibility of the weld metal to hot-cracking. Therefore, it appears that nitrogen should be considered to have a detrimental effect on the weldability of austenitic stainless steels.

Paper presented at the 62nd AWS Annual Meeting held in Cleveland, Ohio, during April 5-10, 1981.

M. J. CIESLAK is the Steel Founder's Society of America Graduate Fellow, and W. F. SAVAGE is Professor of Metallurgical Engineering and Director of Welding Research, School of Engineering, Materials Division, Rensselaer Polytechnic Institute, Troy, New York. A. M. RITTER is a metallurgist, General Electric Corporate Research and Development, Schenectady, New York.

Experimental Procedure

Weldability Testing

The Varestraint Test was used to determine the weldability of the three heats listed in Table 1. Heat 1 is a wrought Type 304L stainless steel. Heats 2 and 3 are CF-8M cast stainless steel.

Heats 1 and 2 were Varestraint tested using both 100% Ar and mixtures of 99%Ar–1%N_2, 97%Ar–3%N_2, and 94%Ar–6%N_2 as the shielding gas in order to determine the influence of nitrogen on the ferrite content and hot-cracking susceptibility of these autogenous welds. Heat 3 was Varestraint tested in a previous study (Ref. 3) using 100% Ar shielding and is included for comparison purposes only. All specimens were tested at 2% augmented strain. The welding variables are listed in Table 2.

Ferrite Measurements

Following Varestraint testing, Magne-Gage readings were taken to determine the ferrite content of the fusion zones. Specimens were examined both on the as-welded surface after wire brushing and within the fusion zone at a location 2-3 mm (0.08-0.12 in.) below the original weld surface. Sections cut from the weld metals with a water-cooled saw were used for subsequent nitrogen analyses.

Twenty Magne-Gage readings were taken for each specimen, and these results were used to establish 95% confidence limits of the mean values of ferrite number using Student's t-test.

Optical and Electron Microscopy

Specimens for optical metallography were removed from Varestraint speci-

Table 1—Compositions of Varestraint Tested Heats, Wt-%

Heat No.	ASTM Type	Cr	Ni	Mo	Mn	Si	C	N	S	P
1	304-L	18.7	9.5	0.31	1.5	0.46	0.024	0.06	0.011	0.034
2	CF-8M	18.2	12.1	2.48	1.2	0.60	0.06	0.05	0.016	0.027
3	CF-8M	19.6	15.4	2.88	0.2	0.38	0.04	0.04	0.025	0.036

mens and were mounted in either a thermosetting resin or epoxy and polished through 0.06 micron alumina. Microstructures were revealed by a 10% oxalic acid electroetch.

Thin foils for TEM/STEM microanalysis were prepared in an electropolishing solution of 20% perchloric acid/80% methanol, using a Fischione twin-jet apparatus. They were examined in the Hitachi H600 TEM operated at 100 kV, and in the JEOL JSEM-200 STEM, operated at 200 kV. Energy dispersive x-ray analyses were performed with a Nuclear Semiconductor detector and a Tracor Northern NS880 analyzer equipped with a PDP11 computer. Peaks of interest were integrated and background counts subtracted using a Tracor Northern software package.

To eliminate as much spurious radiation as possible, a graphite insert was placed in the specimen holder, and the holder was tilted to a 45 deg angle to optimize the count rate (Ref. 12). Raw data for the compositional profiles were generated at steps of 0.1–0.2 μm from the ferrite/austenite interface, usually up to a distance of 2 μm. Spectra beyond this point were taken at spacings of 0.5-1.0 μm, depending on the total distance from the interface. The magnifications at which the data collection was done varied from X20,000 for widely separated readings, to X100,000 for areas close to the interface. The electron beam was approximately 100 Å in diameter, and the instrument was operated in the spot mode. Compositions of the ferrite were obtained from spectra taken in the middle of the ferrite, and often more than one spectrum was obtained.

The x-ray data were rendered into weight-percents using the Cliff-Lorimer equation (Ref. 13) by which composition and integrated intensities are related:

$$\frac{C_A}{C_B} = k_{AB}\frac{I_A}{I_B}$$

where C_A and C_B are the weight fractions of elements A and B, and I_A and I_B are the integrated intensities.

The value of k_{AB} remains essentially constant for an element as long as absorption and fluorescence effects are minimal. This holds for compositions roughly within the stainless steel range for Cr, Fe, Ni, and Mo, if the spectra are taken in regions of foil thicknesses up to approximately 3000 Å. Beyond this thickness, the absorption/fluorescence effects become pronounced, especially for the Mo data. In general, the profiles were obtained in areas where the foils were thin (~2000 Å); therefore, no absorption or fluorescence correction procedures were applied to the data (Ref. 14).

Values for k_{AB} were obtained by taking 10 spectra in each of three grains in two stainless steels of known composition, a Type 304 and a 316 heat. From the mean values calculated, k_{AB} for each element was derived, normalizing on the Fe peak. In the case of Cr, for example, the Cliff-Lorimer equation becomes:

$$\frac{C_{Cr}}{C_{Fe}} = k_{Cr}\frac{I_{Cr}}{I_{Fe}}$$

The Fe concentration is obtained from the formula:

$$C_{Cr} + C_{Ni} + C_{Mo} + C_{Fe} + C_X = 1$$

where C_X is the mole fraction of any other elements, such as Mn, in the steel.

Statistical fluctuations in the values of k_{AB} for each element result in the minimum uncertainty in any reading in the profiling data. Average values of 2-sigma, calculated in areas of constant composition in the austenite are ±0.6 wt-% for Cr, ±0.8 wt-% for Ni, ±1.0 wt-% for Fe and ±1.0 wt-% for Mo. As can be seen, the relative scatter for the Mo is much higher than for the other elements, since the amount of Mo present, and therefore the intensity of the peak, is small.

Two-sigma values are not absolute for any of the elements, as the scatter will tend to increase in regions of lower elemental concentration than the nominal, and decrease in areas richer in a particular element.

Results and Discussion

Nitrogen Pickup

Table 2 and Fig. 1 summarize the effect of adding nitrogen to the argon shielding gas during Varestraint testing. In Fig. 1 an increase in the nitrogen content of the weld metal is seen as the nitrogen content of the shielding gas is increased, a pattern of nitrogen pick-up in agreement with results published by other authors (Ref. 9, 10).

Figure 2 shows the influence of nitrogen additions to the shielding gas on the weld metal Ferrite Numbers. The observed decrease in Ferrite Number with increasing nitrogen content of the shielding gas is consistent with previously published data (Ref. 9-11).

Weldability

The total crack length produced by Varestraint testing on heats 1, 2, and 3 at 2% augmented strain is presented in Fig. 3. Heats 1 and 2 were crack-free when welded using 100% Ar shielding, while heat 3 shows extensive hot-cracking sensitivity even with 100% Ar shielding. As seen in Fig. 2, heats 1 and 2 have weld

Table 2—Effects of Adding Nitrogen to Argon Shielding Gas During Varestraint Testing[a]

Heat no.	Gas composition	Nitrogen in weld metal, wt-%	Current, A	Voltage, V
1	100%Ar	0.063	260	13.5
1	99%Ar-1%N_2	0.131, 0.143	255	14.0
1	97%Ar-3%N_2	0.156	255	13.5
1	94%Ar-6%N_2	0.221	250	13.5
2	100%Ar	0.052	260	13.5
2	99%Ar-1%N_2	0.087	250	14.0
2	97%Ar-3%N_2	0.121	255	13.5
2	94%Ar-6%N_2	0.192	250	13.5
3	100%Ar		300	15.0

[a]Electrode composition – tungsten + 2% thoria; electrode – conical tip, 90 deg included angle; electrode extension from collet – approx. 21/32 in.; electrode diameter – 1/8 in.; arc length approx. 3/32 in. (measured cold); travel speed – 4 ipm; gas flow rate – approx. 40 cfh; current – DCSP; specimen thickness – 1/2 in.

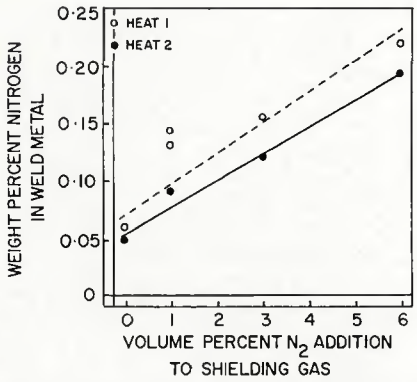

Fig. 1—Nitrogen content of weld metal as a function of nitrogen content of the GTA shielding gas

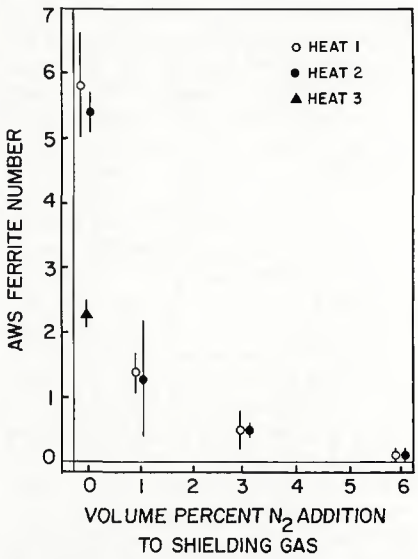

Fig. 2—Ferrite content of weld metals as a function of nitrogen content of the GTA shielding gas

metal Ferrite Numbers of 5.8 and 5.4, respectively, whereas heat 3 has a weld metal Ferrite Number of 2.3.

Figures 4-6 are optical photomicrographs of the fusion zones in heats 1, 2, and 3, respectively, welded using 100% Ar shielding gas. Figures 4 and 5 show that the retained delta ferrite is located at the cores of the original cellular dendrites in heats 1 and 2, indicating that delta-ferrite was the primary phase during solidification of these alloys. In heat 3, the retained ferrite is located at interdendritic volumes (Fig. 6), from which one infers that this alloy solidified with austenite as the primary phase.

Adding nitrogen to the shielding gas caused a decrease in weldability for both heats 1 and 2. A 1% nitrogen addition to the shielding gas resulted in a significant amount of hot-cracking in heat 2, but left heat 1 virtually unaffected. Both heats experienced greater hot cracking tendencies at 3% and 6% nitrogen, although the similarity of data under the two shielding conditions suggests that a saturation level of hot cracking was reached for both alloys at 3% nitrogen. Figure 2 shows that virtually all of the ferrite was eliminated in both alloys at the 6% nitrogen level, as determined by the Magne-Gage technique.

Figures 7 and 8 are characteristic of the duplex microstructure of welds which exhibited significant fusion zone hot-cracking. These weld metals all solidify as primary austenite and contain interdendritic eutectic-ferrite, which formed during the terminal transient stage of solidification. The position of ferrite in these microstructures is similar to that seen in heat 3 (Fig. 6).

We have observed then that a change in the solidification mode from one of primary delta-ferrite to one of primary austenite may be accomplished by the addition of only very small amounts of nitrogen to the shielding gas, and that this change in the mode is accompanied by an increase in the hot-cracking susceptibility of these alloys. It is important to recognize that the concentration of impurity elements, such as sulfur and phosphorus, in heats 1 and 2 was not high enough to cause hot-cracking in

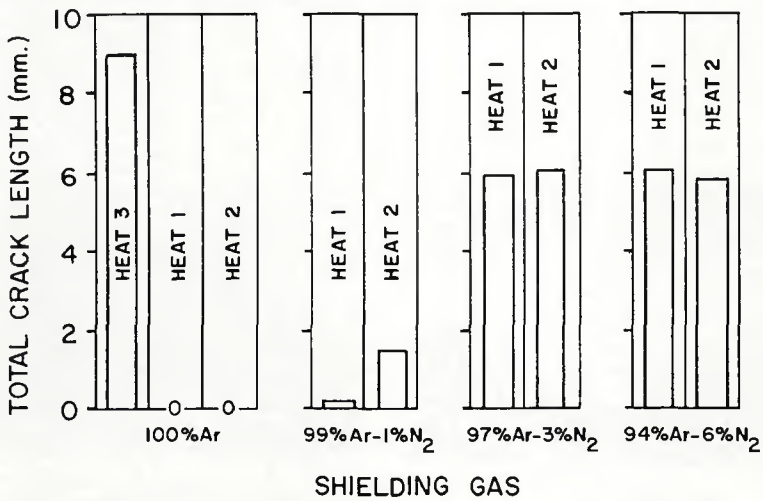

Fig. 3—Varestraint results for heats 1, 2, and 3 using different shielding gases. All tests at 2% augmented strain

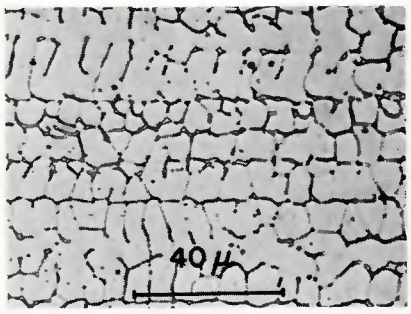

Fig. 4—Optical micrograph of heat 1, welded using 100% Ar shielding gas, showing the vermicular delta-ferrite microstructure typical of the primary delta-ferrite solidification mode

welds which solidified as primary delta-ferrite. On the other hand, considerable hot-cracking occurred in these heats when austenite was made the primary phase during solidification.

Ferrite Morphology

The two forms of ferrite studied in this investigation could be readily distinguished using the TEM. Figure 9 is characteristic of the vermicular ferrite structure resulting from primary delta-ferrite solidification, while Figs. 10 and 11 are examples of interdendritic eutectic-ferrite, found in the hot-crack sensitive welds.

Figure 11 clearly establishes the position of the eutectic-ferrite at the boundaries of the primary austenite cellular-dendrites. The shape of the retained ferrite is seen to change as the solidification mode is changed by the addition of nitrogen to the shielding gas. In the case of primary ferrite, the austenite/ferrite interface is generally rounded, whereas the eutectic-ferrite/austenite interfaces are often sharp or stepped in some planes (Fig. 12). It should be mentioned that diffraction analyses were performed in all samples, in order to confirm the identity of the ferrite phase (Fig. 13).

Another distinguishing feature of eutectic-ferrite is the increased tendency for small precipitates to form at the austenite/eutectic ferrite interface. These can be seen on the stepped interface and at the lower right interface in Fig. 12.

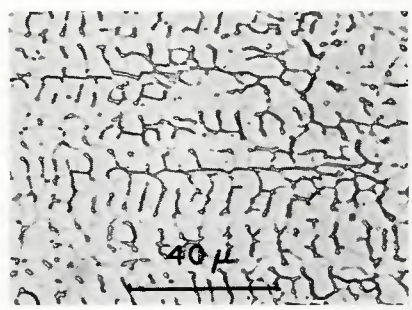

Fig. 5—Optical micrograph of heat 2, welded using 100% Ar shielding gas, exhibiting the vermicular delta-ferrite microstucture characteristic of the primary delta-ferrite solidification mode

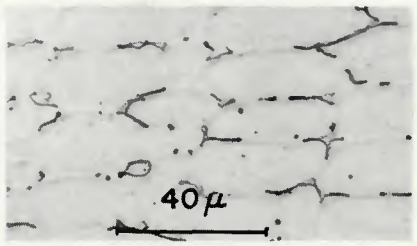

Fig. 6—Optical micrograph of heat 3, welded using 100% Ar shielding gas, showing eutectic-ferrite located at the interstices of primary austenite dendrites

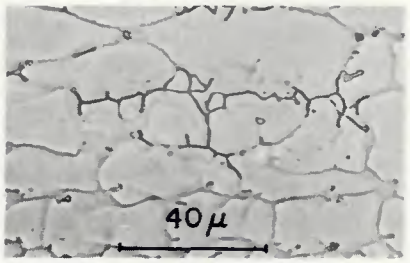

Fig. 7—Heat 1, welded using 97%Ar-3%N_2, showing eutectic-ferrite located between primary austenite dendrites

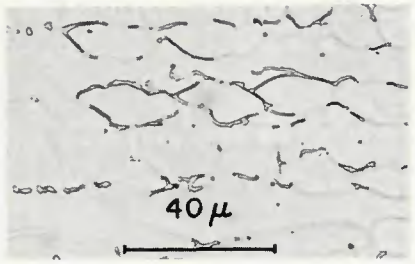

Fig. 8—Heat 2, welded using 97%Ar-3%N_2, exhibiting eutectic-ferrite in interdendritic volumes

Figure 14 shows a dense covering of precipitates on the interphase boundary in this CF-8M alloy. These particular precipitates were found by EDS to be enriched in Cr and Mo with respect to the adjacent ferrite and austenite phases. A similar precipitation phenomenon was seen in the 304-L, although the density of particles appeared to be somewhat less. On the other hand, the ferrite/austenite interfaces in the primary delta ferrite welds are usually free of precipitates (Fig. 15).

The large number of precipitates at the austenite/eutectic-ferrite interfaces is probably caused by the supersaturation of the eutectic-ferrite with elements rejected ahead of the moving austenite/liquid interface during solidification. These elements later nucleate precipitates which grow during the decomposition of the eutectic-ferrite.

Solidification Mechanics

Within the composition limits for a specific type of stainless steel, the balance between ferrite and austenite stabilizers is the major factor controlling the solidification mode. When the ferrite stabilizers are dominant, delta-ferrite is the first solid to crystallize from the liquid; conversely when austenite stabilizers predominate, austenite is the first solid to form from the liquid.

During cooling to room temperature much of the primary delta-ferrite becomes unstable and transforms to austenite. On the other hand, primary austenite remains stable during cooling to room temperature and only the interdendritic eutectic-ferrite, if any exists, partially or totally transforms to austenite.

Primary Delta Ferrite Mode

Studies performed by Lippold (Ref. 5) led to the hypothesis that primary delta-ferrite can transform to austenite by a massive transformation. This involves a polymorphic phase change which occurs during rapid cooling, and is characterized by the fact that the parent (delta-ferrite) and product (austenite) phases have the same chemical composition but differ in crystal structure. This transformation can occur only if the competing diffusion-controlled transformation is inhibited.

Calculations based upon diffusion coefficients reported by several authors (Ref. 15-18) indicate that diffusion-controlled transformations can occur in stainless steels during cooling associated with conventional arc welding processes. Thus, the massive transformation mechanism is unlikely to occur in these alloys unless a welding process is used which would create very high cooling rates, such as those associated with the high energy density processes like electron beam or laser welding.

Since diffusion processes are operative, the microstructure and pattern of microsegregation established during solidification is modified at sub-solidus temperatures. Lippold (Ref. 5) and Arata (Ref. 4) have studied the microstructure and pattern of microsegregation produced by extremely rapid cooling rates. Lippold water-quenched various sized molten droplets of Type 308, 310, and 312 weld metals during GMA welding to achieve theoretical cooling rates of several thousand degrees Centigrade per second. Arata decanted liquid weld metal during GTA welding of Types 304 and 310 stainless steel by applying a high-pressure water-spray quench. Analysis was then performed on the solidification structures present adjacent to the solid-liquid interface at the instant of quenching. Microprobe analyses of the rapidly cooled primary delta-ferrite dendrites in both 308 (Ref. 5) and 304 (Ref. 4) indicated that the delta-ferrite is enriched in chromium, but by less than 2 weight percent over the nominal composition. Also, the nickel content of the delta-ferrite was found to be lower than the nominal composition, but only by approximately 2 wt-%.

On the other hand, STEM analyses performed on conventional GTA welded primary delta-ferrite 304-L and CF-8M specimens during this investigation and by Lyman, *et al.* (Ref. 19) are shown in Figs. 16-18, respectively. These indicate that, during normal continuous cooling to room temperature, the chromium content of the remaining ferrite is increased by 7 to 8 wt-% and the nickel content is decreased by 4 to 6 wt-% relative to the nominal composition. Note that in Fig. 17 the concentration gradient of molybdenum is similar to that of chromium, as both are ferrite stabilizers and tend to segregate in a similar manner.

The observed composition gradients in the austenite and the change in composition of the retained delta ferrite can be explained by reference to the pseudo-binary diagram in the Fe-Cr-Ni system at 70% Fe shown in Fig. 19. Note that both the austenite (γ) and ferrite (δ) solvus lines slope toward higher chromium and lower nickel contents as the temperature is lowered. Within the two-phase ($\delta + \gamma$) region, the ferrite and austenite solvus lines define the composition of the two phases in equilibrium with each other. If the system is at equilibrium, the volume

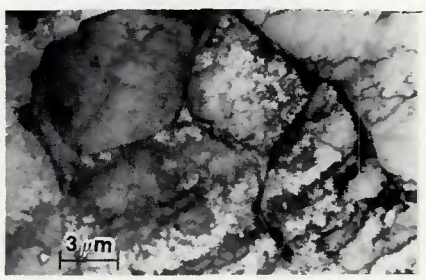

Fig. 9—TEM micrograph of primary delta-ferrite found in heat 1, welded using 100% Ar shielding. Note curved continuous appearance of the ferrite

Fig. 10—TEM micrograph of interdendritic eutectic-ferrite found in heat 2, welded using 99%Ar-1%N_2 shielding gas

Fig. 11—TEM micrograph showing position of eutectic-ferrite at the austenite cellular dendrite boundary in heat 2, welded using 97%Ar-3%N_2 shielding gas

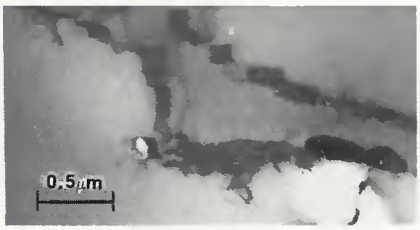

Fig. 12—TEM micrograph of eutectic ferrite found in heat 2, welded using 99%Ar-1%N_2 shielding gas. Note the stepped interphase interface and the precipitates along the interface

Fig. 13—Electron diffraction pattern characteristic of the body-centered-cubic ferrite phase, in this case of a [111] orientation

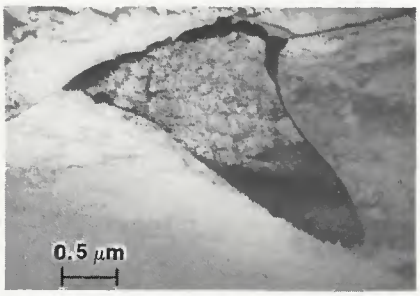

Fig. 14—Precipitates found at the eutectic-ferrite-austenite interface in heat 2, welded using 97%Ar-3%N_2 shielding gas

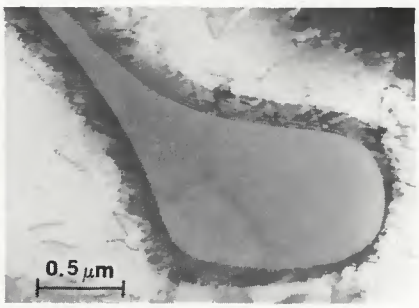

Fig. 15—Precipitate-free interface between primary delta-ferrite and austenite. Heat 2, 100% Ar shielding gas

fraction of each phase may be determined at any temperature using the "tie-line lever law" (Ref. 20). Qualitatively, the diagram implies that, for an alloy of composition C_o, the volume fraction of delta-ferrite decreases and its composition changes toward increasing chromium and decreasing nickel contents as the temperature decreases.

At the cooling rates associated with fusion welding, macroscopic equilibrium is impossible. However, the intercepts of the temperature isotherms with the austenite and ferrite solvi still define the interfacial concentrations of the phases in contact at the moving reaction interface, a phenomenon known as microscopic equilibrium. Diffusion-controlled concentration gradients will be created in each phase as the reaction interface moves into the primary delta-ferrite dendrites.

The distribution of nickel and chromium is shown in schematic form at two different temperatures during non-equilibrium transformation of an alloy of composition C_o (Fig. 20). In Fig. 20A, the interface temperature is assumed to be T_1 and the $\gamma - \delta$ interface is assumed to have migrated from the dendrite interstice toward the dendrite core. According to microscopic equilibrium, the γ and δ in contact at the interface will exhibit compositions shown as the intersection of the T_1 isotherm with the γ and δ solvi, respectively.

Because of the rapid cooling rates, neither the austenite nor the ferrite can be homogeneous and therefore diffusion gradients for both nickel and chromium are seen in both phases. Note that the necessity of maintaining a material balance dictates that the shaded areas on opposite sides of the nominal composition dashed line, C_o, be equal. Figure 20B represents a similar schematic solute distribution for a temperature T_2, at which point austenite has consumed most of the original delta-ferrite. Note that both the austenite and ferrite at the reaction interface have moved to higher chromium content and lower nickel content. Note also that the composition of the retained ferrite has been modified to a higher bulk chromium concentration and lower bulk nickel concentration.

The diffusion model predicts that, within both the ferrite and the austenite, the highest chromium content and lowest nickel content would be at the interphase interface. This results in the shape of the solute gradients shown in Figs. 16–18. Furthermore, high resolution STEM work reported by Lyman (Ref. 19), shows the distribution of chromium and nickel within the retained delta-ferrite after normal cooling to room temperature (Fig. 21). The distribution of solute and the shape of the gradients are in agreement with the diffusion model. A similar profile was reported by David, *et al.* (Ref. 21) for Type 308 weld metal which was slowly cooled to 20°C (36°F) below the solidus temperature and then water quenched. It is important to note that, in this model, both the chromium content of austenite and the ferrite at the moving interface increase as the transformation proceeds.

It should be mentioned that the model is oversimplified since the diagrams imply that nickel and chromium diffuse at the same rates. Actually, chromium diffuses faster than nickel in both phases (Ref. 16-18) and, therefore, the chromium concentration always appears more homogeneous than the nickel concentration in any of the STEM profiles presented. Furthermore, the model assumes that the tie-line across the two-phase field lies strictly in the plane of the pseudo-binary diagram, which is not necessarily true.

Primary Austenite Mode

Rapid quenching experiments performed by Lippold (Ref. 5) and Arata, *et al.* (Ref. 4) on Type 310 stainless steel indicate that both chromium and nickel are rejected to the liquid during primary austenite solidification. The cores of the cellular dendrites are thus depleted in chromium and nickel relative to the nominal composition. Both studies show that chromium segregates more highly than nickel.

During the present investigation, heats of 304-L and CF-8M were made to change their solidification mode from one of primary delta-ferrite to one of primary austenite by the addition of nitrogen to the argon shielding during GTA welding. Figures 22 and 23 summarize the results of STEM analyses performed on these heats. Note that the austenite near the austenite/eutectic-ferrite interface is depleted in iron and enriched in the solute elements chromium, nickel, and molybdenum (where present).

The fact that the retained ferrite is located at the dendrite interstices supports the postulate that it forms from the liquid as a divorced-eutectic phase during the terminal transient stage of solidification. This ferrite forms as a result of solute enrichment at the dendrite interstices during the primary austenite mode of solidification. The behavior is consistent with the general theory of cellular dendritic solidification, in which the composition of liquid in the terminal transient approaches an invariant point, such as a eutectic.

Figure 24 shows similar STEM data for heat 3, which, by virtue of its nominal composition, solidified as primary austenite even when GTA welded using 100% Ar shielding gas. Note the similarity with Figs. 22 and 23.

The 10-15% decrease in the iron content in the austenite over a distance of 2-3 microns on either side of the eutectic ferrite cannot be rationalized in its entirety by any solid-state diffusion mechanism. Rather, it appears likely that this depletion originated as microsegregation during the terminal transient period of solidification and was modified in the direction of equilibrium by diffusion during cooling to room temperature. It is important to note that diffusion processes are more sluggish in austenite than in ferrite, which leads to a greater retention of the microsegregation accompanying primary austenite solidification. Also, since austenite is the stable phase at room temperature, the microstructure and microsegregation of this phase are not altered by phase transformations during cooling to room tem-

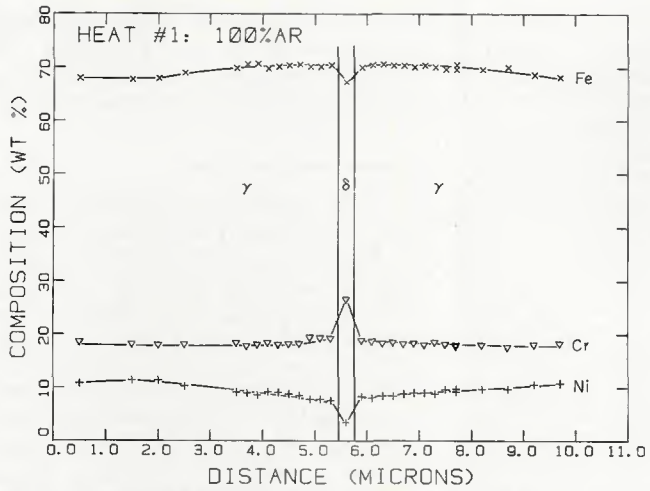

Fig. 16—STEM profile in heat 1, welded using 100% Ar shielding. Weld solidified as primary delta-ferrite

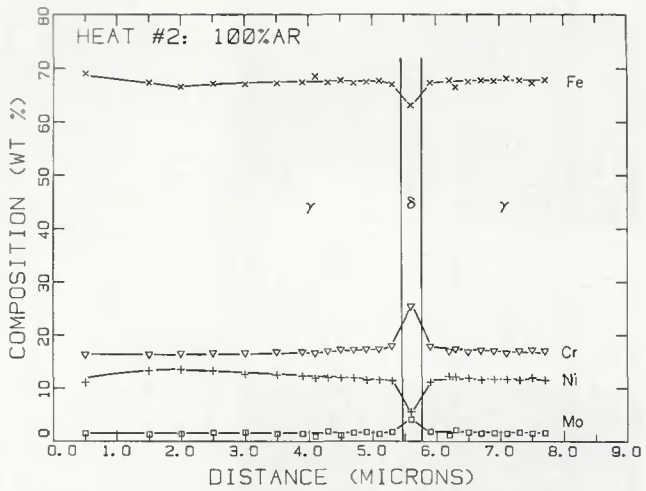

Fig. 17—STEM profile in heat 2, welded using 100%Ar shielding. Weld solidified as primary delta-ferrite

perature.

Under equilibrium conditions these alloys should be fully austenitic at room temperature and so diffusion will occur in such a fashion as to reduce the volume of eutectic-ferrite present. Diffusion of solutes across the original austenite/eutectic-ferrite interface causes a diffusion-controlled migration of the interface into the eutectic-ferrite to convert the outermost layers of eutectic-ferrite to austenite. The composition of this austenite follows the austenite solvus as the temperature decreases. Therefore, the nickel content of the austenite decreases and the chromium and molybdenum contents increase as the interphase-interface moves into the eutectic-ferrite. This behavior is supported by the STEM profiles shown of the austenite near the eutectic-ferrite. However, the high resolution STEM analyses needed to confirm the solute distribution within the retained eutectic-ferrite were not performed during the present investigation.

Arata (Ref. 4), *et al.* and David (Ref. 21), *et al.* have reported that austenite could also form directly from the liquid in welds which initially solidify as primary delta-ferrite. Lippold (Ref. 5) also reported this phenomenon and attributed it to the enrichment of austenitizing elements in the remaining liquid. It is postulated that the microsegregation associated with the solidification of this austenite is similar to that associated with any primary austenite solidification process.

Summary of Solidification Modes

Based upon previously published data (Ref. 3,4,5,10,19,21) and the results of this study, it appears that four modes of solidification are possible in Fe-Cr-Ni stainless steels:

(a) Solidification completely to delta-ferrite.

(b) Solidification completely to austenite.

(c) Solidification as austenite with the formation of a divorced eutectic-ferrite at the dendrite interstices during the terminal transient stage of solidification.

(d) Solidification as delta-ferrite until partitioning of austenitizers to the remaining liquid causes this liquid to solidify as austenite.

The distribution of solute elements resulting from solidification in each of the four modes listed above is postulated to occur as shown schematically in Figs. 25 A, B, C, and D, respectively. In each of these figures the dashed lines representing the chromium and nickel distributions at the solidus temperature are referred to the nominal compositions which are shown as solid horizontal lines, labelled Cr_o and Ni_o, respectively. Growth is assumed to have occurred from left to right, and the abscissa represents the location within the dendrite from the core at the left to the interstice at the right.

Figure 25A indicates that, during solidification completely to ferrite, the dendrite cores are Cr enriched and Ni depleted, while the interdendritic volumes are Cr depleted and Ni enriched as must be necessary to insure a material balance. Figure 25B shows that, during solidification totally to austenite, the dendritic cores are depleted in both Cr and Ni and that the interdendritic regions are enriched in these elements, but not enough to form eutectic-ferrite.

Figure 25C shows a situation similar to Fig 25B, except that the nominal compo-

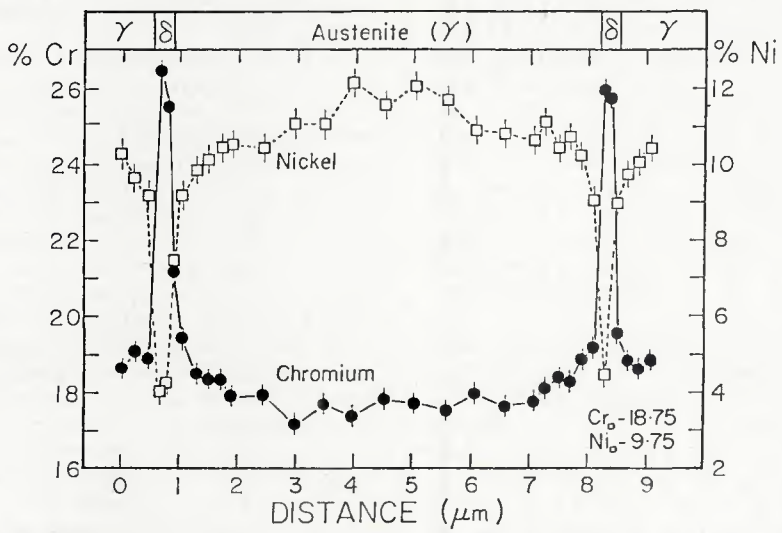

Fig. 18—STEM profile, after Lyman, et al. *(Ref 19), of primary delta-ferrite weldment*

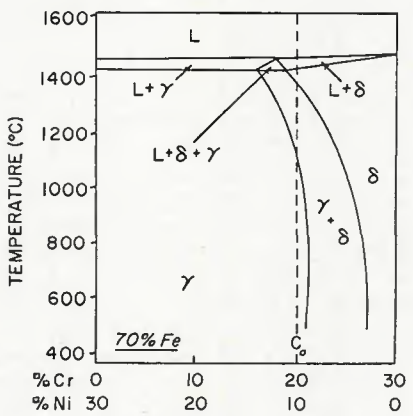

Fig. 19—Pseudo-binary diagram in the Fe-Cr-Ni system at 70% Fe

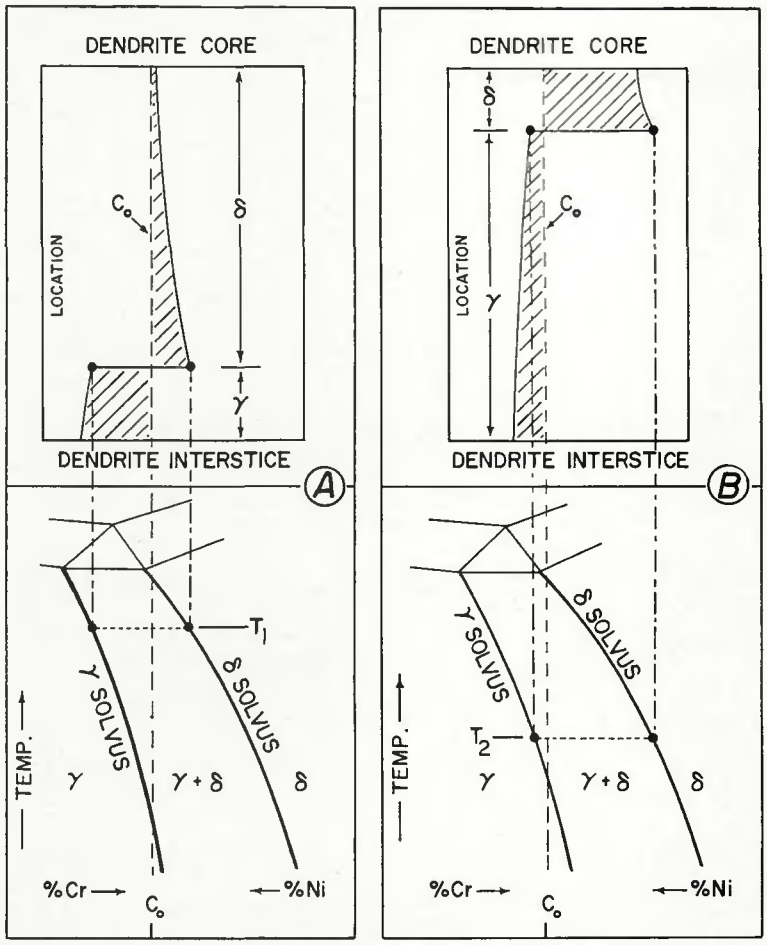

Fig. 20—Schematic representations of the diffusion-controlled ferrite-to-austenitic transformation: A—at temperature T_1; B—continuation of the transformation as temperature is lowered to T_2

sition and microsegregation in this primary austenite case are such that eutectic-ferrite forms at interdendritic volumes. The eutectic-ferrite will have a higher Cr content and a lower Ni content than the adjacent austenite, which gives rise to the sharp compositional discontinuity at the interface. Figure 25D shows the elemental distribution postulated during solidification of primary delta-ferrite duplex alloys of Types 304, 304-L, 308, 308-L, 316, 316-L, and their cast counterparts. The dendrite cores are enriched in Cr and depleted in Ni.

Solidification continues as delta-ferrite until the liquid is so enriched with austenitizers and depleted of ferritizers that austenite now solidifies from the liquid. This austenite is postulated to grow in a manner described in Fig. 25B. The initial austenite is depleted in both Cr and Ni relative to the adjacent delta-ferrite and the composition changes discontinuously across the interface. The rejected solute again ends up in interdendritic volumes. The magnitude of this enrichment will depend upon the nominal composition and the extent of microsegregation determined by welding and solidification parameters.

The specimens analyzed by STEM/EDS techniques in this study showed no eutectic-ferrite in the primary delta-ferrite welds. It must be recognized that Fig. 25 is schematic in form only and that diffusion will modify the composition during continuous cooling to room temperature.

Conclusions

1. Heats 1 and 2 solidified as primary delta-ferrite when GTA welded using 100% Ar shielding. Heat 3 solidified as primary austenite when GTA welded using 100% Ar shielding.

2. Based upon metallographic analysis and STEM elemental profiles, Heat 1 solidified as primary delta-ferrite and heat 2 solidified as primary austenite when GTA welded using 99% Ar-1% N_2 shielding. Heat 1 experienced only very little hot-cracking whereas heat 2 showed extensive hot-cracking under these conditions. Heat 2 contained eutectic-ferrite and heat 1 did not.

3. Heats 1 and 2 solidified as primary austenite and both contained eutectic-ferrite when GTA welded using 97%Ar-3%N_2 shielding. Both heats experienced extensive hot-cracking when welded under these conditions.

4. Both heats 1 and 2 solidified as primary austenite and were essentially ferrite-free when GTA welded using 94%Ar-6%N_2 shielding. Both hot-cracked extensively, but the similarity of the data to that for 97%Ar-3%N_2 specimens suggests that a saturation level of hot-cracking was reached before the microstructure became wholly austenitic.

5. Varestraint results show that a change in solidification mode from primary delta-ferrite to primary austenite results in an increase in hot-cracking sus-

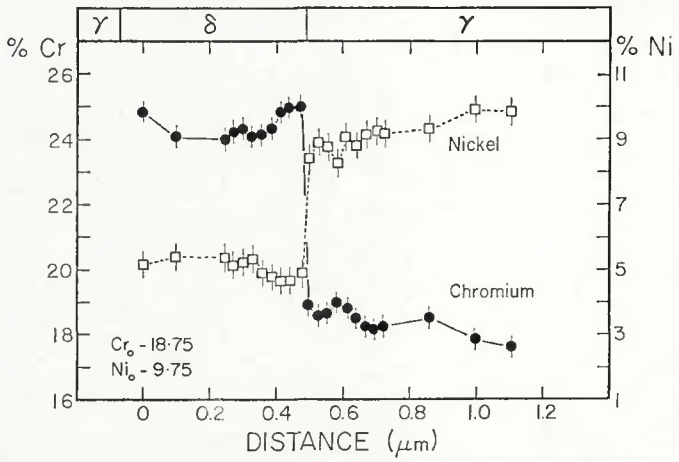

Fig. 21—High resolution STEM profile, after Lyman, et al. (Ref. 19) in a primary delta-ferrite weldment. Note that within the ferrite and the austenite, the highest Cr content and the lowest Ni content occurs at the interface

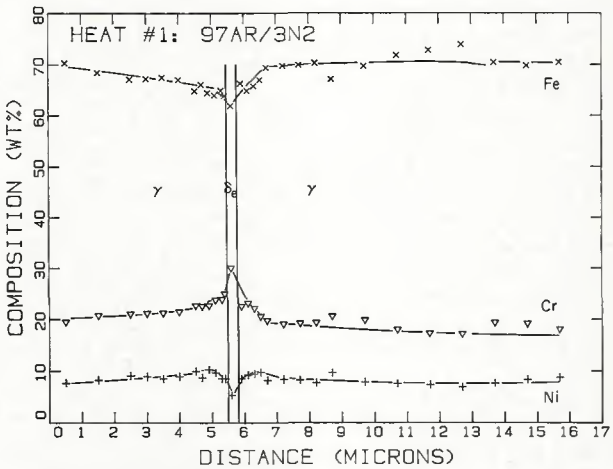

Fig. 22—STEM profile in heat 1, welded using 97%Ar-3%N_2 shielding gas, containing eutectic-ferrite, δ_e

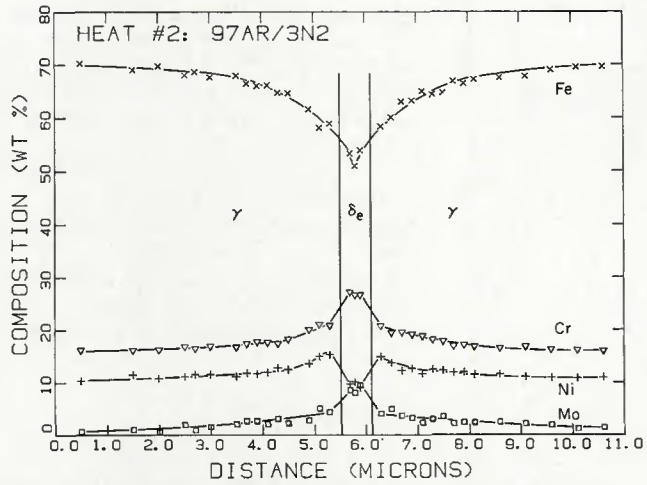

Fig. 23—STEM profile in heat 2, welded using 97%Ar-3%N_2 shielding gas, containing eutectic ferrite, δ_e

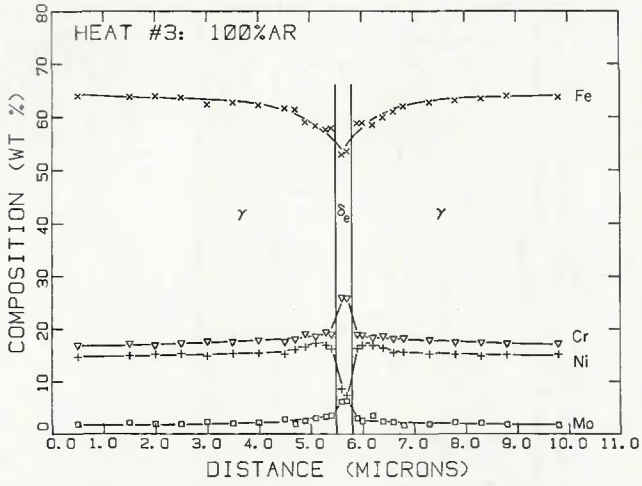

Fig. 24—STEM profile in heat 3, welded using 100%Ar shielding gas, containing eutectic-ferrite, δ_e

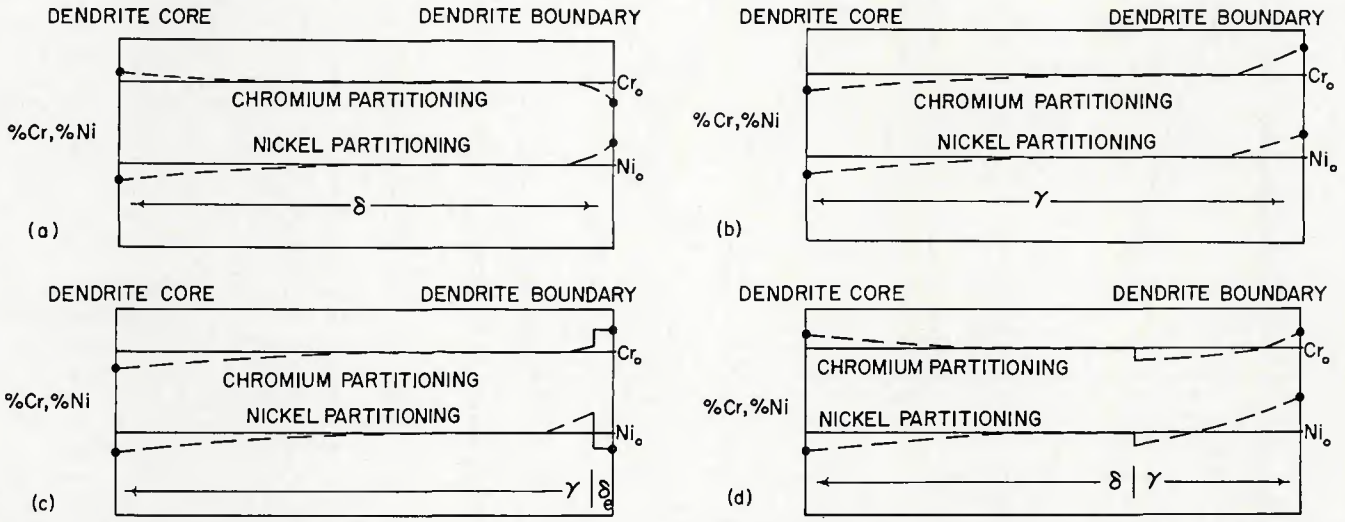

Fig. 25—Schematic distribution of Cr and Ni found during solidification of stainless steels: (a) solidification completely to delta-ferrite, (b) solidification completely to austenite, (c) solidification as primary austenite with the formation of divorced eutectic ferrite, (d) solidification beginning as primary delta-ferrite and concluding as austenite

ceptibility in these alloys.

6. Eutectic-ferrite may be formed at the dendrite interstices in some alloys which solidify as primary delta-ferrite. Eutectic-ferrite can be distinguished from primary delta-ferrite at room temperature in three ways: the position of ferrite in the microstructure, the occurrence of precipitates on the eutectic-ferrite/austenite interfaces, the difference in elemental STEM profiles.

7. Extensive stick-out (electrode extension) or arc length may result in the aspiration of atmospheric nitrogen in the welding arc which could cause an increase in the hot-cracking susceptibility of normally primary delta-ferrite duplex stainless steels.

8. Four modes of solidification are possible in Fe-Cr-Ni stainless steels:

a. solidification totally to delta-ferrite.

b. Solidification totally to austenite.

c. Solidification as primary austenite with the formation of divorced eutectic-ferrite in interdendritic volumes.

d. Solidification as primary delta-ferrite until the remaining liquid becomes sufficiently enriched in austenitizers to solidify in a primary austenite mode.

9. The solid-state ferrite-to-austenite transformation is diffusion-controlled and may be modelled with the aid of Fe-Cr-Ni pseudo-binary phase diagrams.

References

1. Borland, J. C. and Younger, R. N. 1960 (Jan). *British Welding Journal:* 22-59.

2. Hull, F. C. 1967. *Welding Journal* 46(9): 399-s to 409-s.

3. Cieslak, M. J., and Savage, W. F. 1980. *Welding Journal* 59(5): 136-s to 146-s.

4. Arata, Y., Matsuda, F., and Katayama, S. 1976. *Trans. of JWRI* 5(2): 35-51.

5. Lippold, J. C., and Savage, W. F. 1980. *Welding Journal* 59(12): 362-s to 374-s.

6. DeLong, W. T., Ostrom, G. A., and Szumachowski, E. R. 1956. *Welding Journal* 35(11): 521-s to 528-s.

7. Long, C. J. and DeLong, W. T. 1973. *Welding Journal* 52(7): 281-s to 297-s.

8. Kotecki, D. J. 1978. *Welding Journal* 57(4): 109-s to 117-s.

9. Baeslack, W. A. III, Savage, W. F., and Duguette, D. J., *Welding Journal* 58(3): 83-s to 90-s.

10. Arata, Y., Matsuda, F., and Saruwatari, S. 1974. *Trans. of JWRI* 3(1): 79-88.

11. Lundin, C. D., Chou, C.-P.D., and Sullivan, C. J., *Welding Journal* 59(8): 226-s to 232-s.

12. Ritter, A. M., Morris, W. G., and Henry, M. F. 1979. *Scanning electron microscopy/*I: 121-126.

13. Cliff, G., and Lorimer, G. W. 1972. *Proc. Fifth Eur. Congress on E.M.:* 140-141.

14. Goldstein, J. I., Costley, J. L., Lorimer, G. W., and Reed, S. J. B. 1977. *Scanning electron microscopy/*I: 315-324.

15. Alberry, P. J., and Haworth, C. W. *Metal Science,* 1974, Vol. 8, p. 407.

16. Hancock, G. F., and Leak, G. M., *Metal Science,* 1967, Vol. 1, p. 33.

17. Perkins, R. A., Podgett, R. A., and Tunala, N. K. 1973. *Met. Trans.* 4(11): 2535-3540.

18. Perkins, R. A. 1973. *Met. Trans. 4(7): 1665-1669.*

19. Lyman, C. E. 1979. *Welding Journal* 58(7): 189-s to 194-s.

20. Reed-Hill, R. E. 1973. *Physical metallurgy principles:* 527. D. Van Nostrand Company.

21. David, S. A., Goodwin, G. M., and Braski, D. N. 1979. *Welding Journal* 58(11): 330-s to 336-s.